

# Experimental Measurement of the Berry Curvature from Anomalous Transport

Martin Wimmer,<sup>1,2</sup> Hannah M. Price,<sup>3</sup> Iacopo Carusotto,<sup>3</sup> and Ulf Peschel<sup>2,\*</sup>

<sup>1</sup>*Erlangen Graduate School in Advanced Optical Technologies (SAOT), 91058 Erlangen, Germany*

<sup>2</sup>*Institute of Solid State Theory and Optics, Abbe Center of Photonics,  
Friedrich-Schiller-Universität Jena, Max-Wien-Platz 1, 07743 Jena, Germany*

<sup>3</sup>*INO-CNR BEC Center and Department of Physics,  
University of Trento, via Sommarive 14, 38123 Povo, Italy*

(Dated: May 12, 2022)

Geometrical properties of energy bands underlie fascinating phenomena in a wide-range of systems, including solid-state materials, ultracold gases and photonics. Most famously, local geometrical characteristics like the Berry curvature can be related to global topological invariants such as those classifying quantum Hall states[1] or topological insulators[2, 3]. Regardless of the band topology, however, any non-zero Berry curvature can have important consequences, such as in the semi-classical evolution of a wave packet[4, 5]. Here, we experimentally demonstrate for the first time that wave packet dynamics can be used to directly map out the Berry curvature. To this end, we use optical pulses in two coupled fibre loops to study the discrete time-evolution of a wave packet in a 1D geometrical “charge” pump, where the Berry curvature leads to an anomalous displacement of the wave packet under pumping. This is both the first direct observation of Berry curvature effects in an optical system, and, more generally, the proof-of-principle demonstration that semi-classical dynamics can serve as a high-resolution tool for mapping out geometrical properties.

The Berry curvature is a geometrical property of an energy band, which plays a key role in many physical phenomena as it encodes how eigenstates evolve as a local function of parameters[5]. In a quantum Hall system, for example, the integral of the Berry curvature over the Brillouin zone determines the Chern number: a global topological invariant that underlies the quantization of Hall transport for a filled energy band[1]. More generally, a local non-zero Berry curvature can have striking physical effects also whenever a band is only partially filled, regardless of whether the global band topology is non-trivial. In the simplest case, a semi-classical wave packet moves under an external force with an additional “anomalous” Hall velocity due to the Berry curvature at its center-of-mass momentum[4, 5]. Now, thanks to recent advances, it has become possible to directly measure such transport with high-resolution by going beyond solid-state materials to other systems such as ultracold atoms and photonics.

In recent years, there have been many landmark experiments to engineer and study geometrical and topological energy bands in ultracold gases and photonics [6–25]. In photonics, for example, topological edge states have been studied in a wide-variety of systems, including photonic crystals[7–9], propagating wave-guides[10, 11], quantum walks[12] and silicon ring resonators[13, 14]. However, while the existence of such edge states is linked to the non-trivial global topological properties of bulk bands, a direct measurement of the Berry curvature itself has so far not been realised. In ultracold atoms, instead, there has been much progress in this direction, for example, with experiments exploiting the effects of Berry curvature on particle transport to extract the Chern number[17], to determine topological phase diagrams[18] and to observe both quantized[21, 22] and geometrical[23]

“charge” pumping. An important final milestone still to be achieved in any system, however, is to use the anomalous transport to map out the Berry curvature over an energy band[5, 26] and so to fully characterise geometrical properties from dynamical effects.

In this Letter, we go beyond previous experiments and demonstrate a full tomography of the Berry curvature of a geometrical energy band from measurements of the anomalous displacement of a wave packet. In our set-up, pulses are injected into two coupled optical fiber loops, so that the temporal evolution of the outgoing pulse-train envelope simulates a wave packet in a 1D “photonic mesh lattice”[27, 28]. We then use a phase modulator in one loop to engineer 2D Floquet bands parameterised by a 1D Bloch momentum and the amplitude of the phase modulation. By slowing ramping the latter, we realize a geometric “charge” pump in which the wave packet is affected by an anomalous velocity due to the Berry curvature. Our high-resolution observation of the wave packet dynamics allows us to map out the Berry curvature for an energy band for the first time in an optical system. This direct mapping of the Berry curvature complements existing methods in ultracold gases to reconstruct the Berry curvature from the measurement of eigenstates via band-projection[24] or using Wilson lines[25]. By bringing geometrical energy bands into the new setting of photonic mesh lattices, our work opens up new opportunities for engineering novel systems also with topology, gain or loss, which may then be studied via wave packet dynamics.

In our experiment, we employ a time-multiplexing, linear optical scheme based on two coupled fiber loops of different lengths[27, 28] (see Fig. 1a). At the beginning of each measurement, an optical pulse is injected into the longer loop before being split by a 50/50 coupler into one pulse in each loop. After every round-trip,

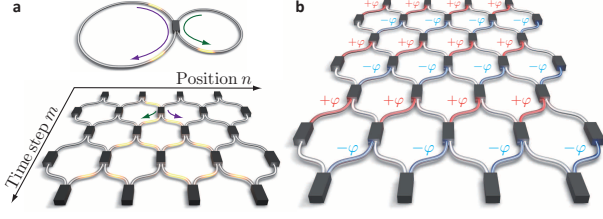


Figure 1. Generation of photonic mesh lattices. a, Optical pulses propagating along two coupled fiber loops of different lengths are used to simulate light evolution on a 1+1D lattice spanned by a discrete time  $m$  and position  $n$ . A roundtrip in the short loop stands for the motion from North West to South East in the lattice, while the propagation from North East to South West in the lattice is equivalent to a roundtrip through the long loop. b, In the short loop, we apply an additional phase modulation with alternating sign at each time step to engineer nontrivial geometrical energy bands (see Fig. 2).

each pulse is again split into two, although due to the different loop lengths, the short loop pulse completes the round-trip before that in the long loop. This time-delay generates a train of pulses over time where each pulse can be labelled by integers  $(m, n)$ , with  $m$  being the total number of round-trips and  $n$  counting how many more round-trips were made in the long compared to the short loop. Based on this labelling  $(m, n)$ , the evolution can be mapped to a 1+1 dimensional lattice as depicted in Fig. 1b, where  $m$  is the number of discrete time steps on the vertical axis, and  $n$  is the position along the horizontal axis, which can either increase or decrease by one at each time step.

In our set-up, the evolution between each time-step is:

$$u_n^{m+1} = \frac{1}{\sqrt{2}}(u_{n+1}^m + i v_{n+1}^m) e^{+i\Phi(m)} \quad (1a)$$

$$v_n^{m+1} = \frac{1}{\sqrt{2}}(v_{n-1}^m + i u_{n-1}^m), \quad (1b)$$

where  $u_n^m$  and  $v_n^m$  are the pulse amplitudes in the short and long loop at position  $n$ . Here we have assumed that the pulse shape does not depend on the specific route taken. In the short loop, we insert an additional phase modulator that will generate the non-trivial geometrical Berry curvature through the time-dependent phase shift  $\Phi(m)$  as discussed in the following and in the Supplementary Information.

Without the phase-shift  $\Phi(m)$ , the above evolution equations are periodic under a double-step in the time-step  $m \rightarrow m + 2$  and the position  $n \rightarrow n + 2$ . Guided by the tight-binding analogy above, we apply the so-called Floquet-Bloch ansatz for the eigenstates[27, 29]

$$\begin{pmatrix} u_n^m \\ v_n^m \end{pmatrix} = \begin{pmatrix} U \\ V \end{pmatrix} e^{-im\theta/2} e^{inQ/2} \quad (2)$$

where the parameter  $Q$  is the “Bloch momentum” along the 1D lattice and  $\theta$  is the propagation constant or

“quasi-energy”. Here, the periodic part of the eigenstates in the  $j$ -th band is denoted by  $\psi_j = (U, V)^T$  and the quasi-energy band structure satisfies[29]

$$\cos \theta = \frac{1}{2}(\cos Q - 1) \quad (3)$$

leading to two bands that are periodic in both  $Q$  and  $\theta$  as expected in a Floquet system, with a band-touching at the edge of the 1D Brillouin zone where  $Q = \pm\pi$  (see Supplementary Note S2).

We can engineer the time-dependent phase-shift  $\Phi(m)$  to realize energy bands with nontrivial geometrical properties, by, for example, cyclically applying a positive phase  $+\varphi$  for even time steps and  $-\varphi$  for odd (see Fig. 1b). Experimentally, this means switching the sign of the phase modulation every time that all pulses complete another round-trip. As the double-step periodicity is maintained, we again use the above ansatz Eq. (2) and find two bands satisfying

$$\cos \theta = \frac{1}{2}(\cos Q - \cos \varphi), \quad (4)$$

as plotted in Figs. 2a,b (see also Supplementary Information). As the eigenstates now depend on both the Bloch momentum  $Q$  and the phase amplitude  $\varphi$ , we can define the Berry curvature characterising the eigenstates in a given band5:

$$\Omega_j^{\varphi, Q} = \frac{\partial}{\partial \varphi} \left\langle \psi_j \left| \frac{\partial}{\partial Q} \right| \psi_j \right\rangle - \frac{\partial}{\partial Q} \left\langle \psi_j \left| \frac{\partial}{\partial \varphi} \right| \psi_j \right\rangle \quad (5)$$

As shown in Figure 2c, the Berry curvature is singular at points where the two bands touch but otherwise can take large non-zero positive and negative values across the 2D parameter space.

To probe the Berry curvature, we prepare a semiclassical wave packet by exciting a superposition of states in one band with a well-defined mean Bloch momentum  $Q$  and with a narrow momentum spread. This can be achieved in good approximation by initially generating a chain of pulses with a Gaussian envelope in the short and long loop, and by setting the correct phase modulation between the envelopes in both loops[30]. Under an external force, the general theory predicts that the wave packet velocity will acquire an anomalous contribution due to the local Berry curvature[4, 5]. In our experiment, this force is simulated by slowly increasing the magnitude of the phase modulation after every second time step, i.e. by slowly “pumping” the phase parameter. We distinguish therefore between two discrete time scales; firstly, there is the fast time scale  $m$  introduced above over which the sign of the phase varies

$$\Phi(M(m)) = \begin{cases} -\varphi(M(m)) & \text{odd } m \\ +\varphi(M(m)) & \text{even } m \end{cases} \quad (6)$$

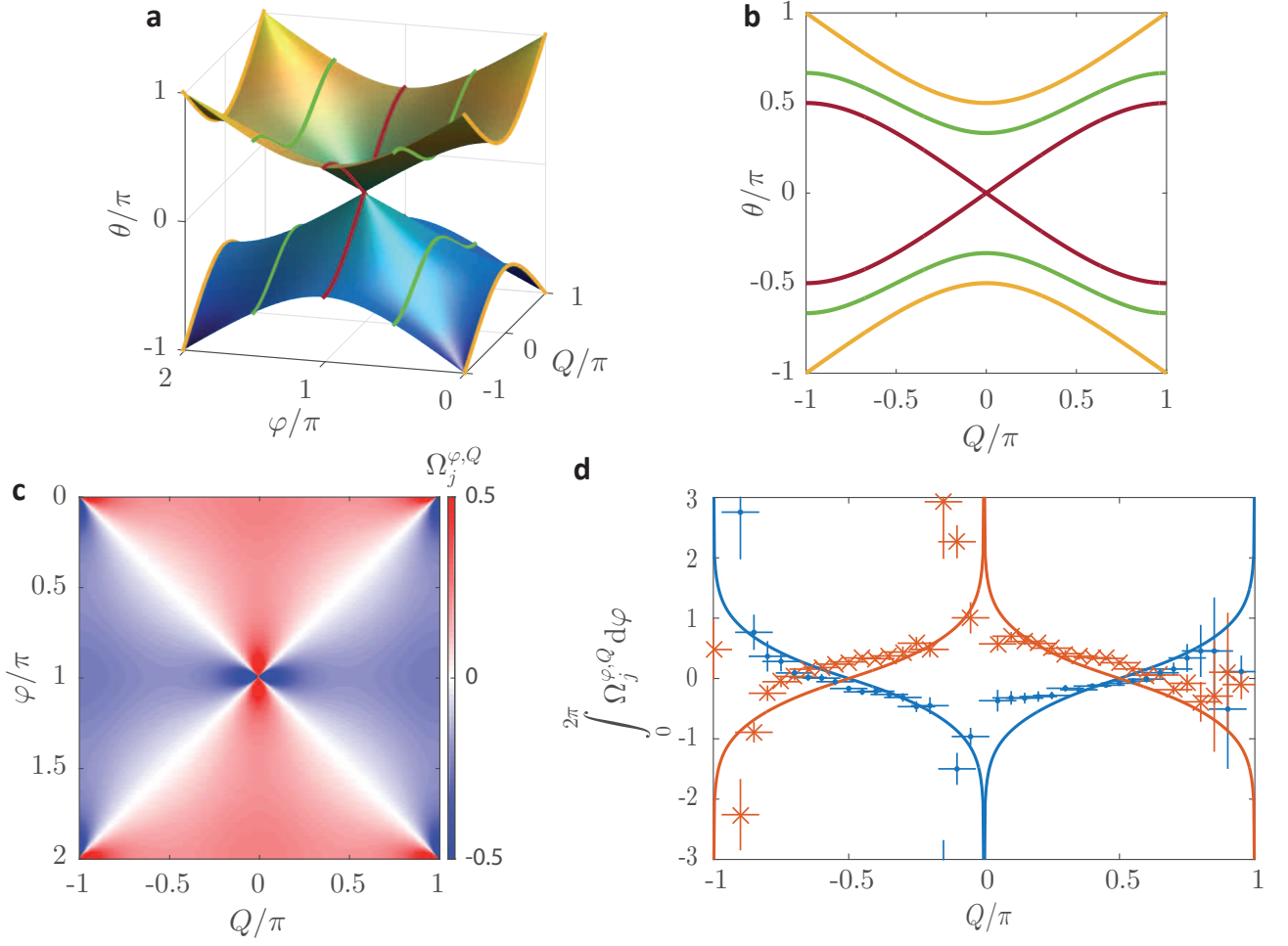


Figure 2. Anomalous transport of a wave packet. a, Band structure of the system as a function of the phase modulation  $\varphi$  and Bloch momentum  $Q$ . Due to the temporal periodicity of the system after two round trips, the band structure is also periodic in  $\theta$ . b, Cut through the band structure for  $\varphi = 0$  (yellow),  $\varphi = \pi/2$  (green) and  $\varphi = \pi$  (red). c, Calculated Berry curvature for the upper band ( $\theta > 0$ ); this is singular at the isolated points where the two bands touch at the center and at the corners of the Brillouin zone. d, By applying Eq. (10), we extract the integrated Berry curvature over each full experimental trajectory from  $\varphi = 0$  to  $\varphi = 2\pi$  (the results for the upper band are marked in orange and for the lower band in blue). For Bloch momenta in the vicinity of  $Q = 0, \pm 1$ , the trajectory approaches a band-touching point, and so adiabaticity breaks down and the protocol fails.

and secondly, there is a slower time scale  $M(m) = \lfloor m/2 \rfloor$ , corresponding to the number of modulation periods, over which the phase magnitude varies

$$\varphi(M(m)) = \varphi_0 M(m) \quad (7)$$

where hereafter we drop the explicit dependence on  $m$ . Note that the fast phase variation in Eq. (6) is directly included in the bands thanks to the ansatz in Eq. (2), while the slow variation in Eq. (7) then adiabatically “pumps” the system along a trajectory in the 2D parameter space, provided that the rate  $\varphi_0$  is sufficiently small compared to the band-gap.

Experimentally, a non-zero Berry curvature shifts the center-of-mass of the Gaussian envelope along the “position”  $n$  as a function of the number of modulation periods

$M$  according to

$$n_j^{\varphi_0}(M) = \int_0^M \left[ v_j^G(\varphi(M'), Q) + \varphi_0 \Omega_j^{\varphi(M'), Q} \right] dM', \quad (8)$$

for a wave packet prepared in the  $j$ -th band with mean Bloch momentum  $Q$  (see Supplementary Information). Here, the second term corresponds to the anomalous velocity due to the Berry curvature while the first is the usual group velocity from the band structure

$$v_j^G(\varphi(M), Q) = \frac{\partial}{\partial Q} \theta_j(\varphi(M), Q). \quad (9)$$

Note that this semi-classical approach necessarily fails close to the band degeneracies where adiabaticity fails;

we therefore restrict the range of Bloch momenta considered to avoid these points.

To cleanly separate Berry curvature from group velocity effects, we apply a variant of the “time-reversal” protocol[26] and compare the propagation (see Fig. 3a) under  $+\varphi_0$  and  $-\varphi_0$  to find

$$\Delta n_j(M) = n_j^{+\varphi_0}(M) - n_j^{-\varphi_0}(M) = 2\varphi_0 \int_0^M \Omega_j^{\varphi(M'),Q} M' dM' \quad (10)$$

where we have used that, for this modulation,  $v_j^G(\varphi, Q) = v_j^G(-\varphi, Q)$  and  $\Omega_j^{\varphi,Q} = \Omega_j^{-\varphi,Q}$  (see Supplementary Information S4 and S5). In this way, we directly measure the integrated Berry curvature over a complete phase-pumping cycle as shown in Fig. 2d. Note that this anomalous displacement can become very large as we approach the band-touching points where the Berry curvature diverges and adiabaticity breaks down; experimentally we measure an anomalous displacement of up to approximately 2 positions over 200 time steps for a wave-packet centered around  $Q = 0.95\pi$  subject to a phase-gradient of  $\varphi_0 = \pi/100$ . The general applicability of this method is further confirmed in the Supplementary Information S8, where the same experimental protocol is applied to a second example of modulation and pumping sequence.

As the most important advance of our work, the wave-packet evolution can be measured after each discrete time-step, allowing for unprecedented high time-resolution of the dynamics. We exploit this to map out the local Berry curvature directly from anomalous transport for the first time, by performing a discrete differentiation of the lateral shift  $\Delta n_j(M)$  as

$$\Omega_j^{\varphi(M),Q} = \frac{\Delta n_j(M+1) - \Delta n_j(M-1)}{4\varphi_0} \quad (11)$$

The result of this procedure is shown in Fig. 3; as can be seen, the main features of the Berry curvature are well captured, such as the overall symmetry and sign, the quantitative magnitude over much of the band and the predicted complementarity of the two bands[5, 24] (i.e.  $\Omega_1^{\varphi,Q} = -\Omega_2^{\varphi,Q}$ ). The observed deviations occur, as expected, after the wave packet has passed near band-degeneracies where adiabaticity breaks down.

In conclusion, we have demonstrated that anomalous wave packet dynamics can provide an important experimental tool for mapping out the local geometrical properties of energy bands. This versatility of this scheme should allow it to be applied in a variety of configurations, including systems with gain and loss[27] and/or nontrivial topological invariants. In the presence of nonlinearities, this technique could provide a new approach for the creation and manipulation of different wave packet structures, such as solitons. Given its simplicity, our experimental set-up also holds the promise of transferring geo-

metrical and topological concepts into the applied world of optoelectronics.

## Methods

A detailed description of the experimental platform is included in the Supplementary Material Note 1. To reduce the noise limit of the data acquisition, the measured propagation was averaged over approximately 10 realizations. For each band, we sequentially prepared wave packets with an initial mean Bloch momentum  $Q$ , which was scanned from  $-\pi$  to  $\pi$  in steps of  $0.05\pi$ . For each value of  $Q$ , we performed measurements for  $-\varphi_0$  and  $+\varphi_0$  before then setting a new value of  $Q$ .

In order to start with a spatially broad and thus spectrally narrow distribution at a specific Bloch momentum  $Q$ , a single seed pulse is injected into the fiber loop system. By switching off one of the two loops in a cyclic fashion after every second time step  $m$ , the system is converted into a lossy mesh lattice as discussed in 30. The resulting propagation is given by a diffusion equation leading to a coherent splitting of the initial pulse into a chain of pulses with a Gaussian envelope. Due to this diffusive motion, the width of the resulting wavepacket grows  $\propto \sqrt{m}$ . Thus, for 200 time steps a wavepacket with a width of  $\approx 6$  positions with respect to the FWHM of the intensity is generated, which provides a sufficiently small spectral width  $\Delta Q \approx 0.07\pi$  to map out the local Berry curvature.

To excite a specific Bloch momentum  $Q$ , we apply a phase of  $\varphi = Q$  during the diffusive motion and a phase of  $\varphi = (Q \pm \pi)/2$  for the last time step before the actual propagation. The choice of the sign allows for a selection of either the upper or the lower band. As discussed in [30, 31], in this way, the appropriate eigenstate corresponding to a Bloch momentum  $Q$  is excited. After the preparation of the Gaussian beam over the first 200 time steps, there is no further switching-off of either loop and, instead, we measure the wave packet dynamics during the next 200 time steps, using the phase modulator to adiabatically “pump” the system as discussed in the main text.

The center-of-masses of the wave packets were extracted by fitting Gaussian distributions to the cross-sections for each time step. A detailed explanation of this fitting procedure, together with examples, is included in Supplementary Material Note 6.

The errorbars depicted in Fig. 2d are estimated by the spectral width  $\Delta Q \approx 0.07\pi$  of the initial excitation in horizontal direction and by the uncertainty of the fit procedure for a 95% confidence level in the vertical direction.

For the full reconstruction of the Berry curvature, it is necessary to differentiate the measured integrated Berry curvature with respect to the time step  $m$  as discussed in Eq. (11). Directly before evaluating the derivative, a

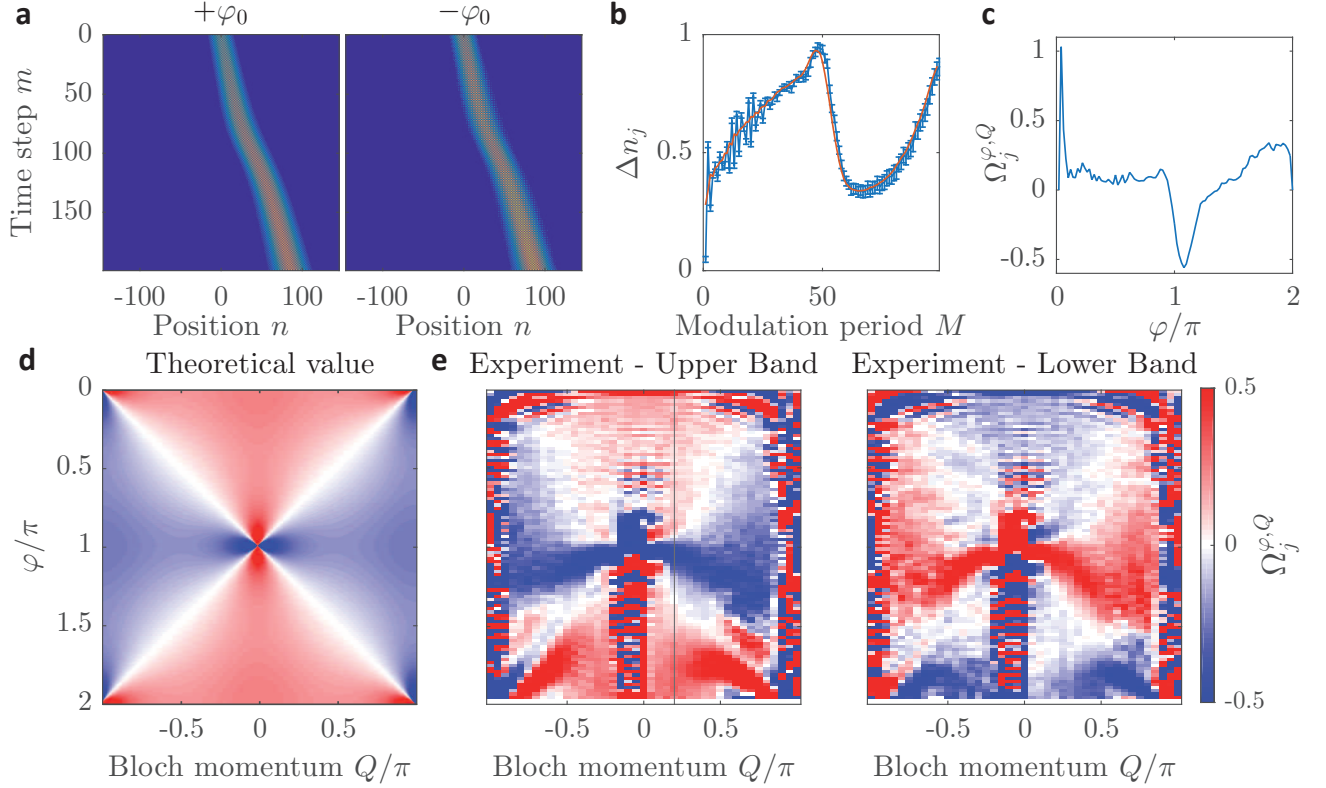


Figure 3. Experimental reconstruction of the Berry curvature. a, Measured propagation of wave packets populating the upper band for  $Q = 0.2\pi$  for  $\pm\varphi_0$ . The center-of-masses are extracted by Gaussian fits for each time step  $m$  and are subtracted for determining the shift of the wave packet due to the anomalous velocity (b). Before numerically differentiating the measured curve (blue line) in (b), a moving average filter with a span of 5 time steps is applied (orange line). The derivative of the averaged signal in (b) is depicted in (c) and represents a cut through the Berry curvature for  $Q = 0.2\pi$  for the phase amplitude  $\varphi$  as indicated by the grey solid line in panel (e). Compared to the theoretical value in (d) the experimental results in (e) for the upper and lower band are in a very good agreement and also illustrate the relation of the Berry curvature  $\Omega_1^{\varphi,Q} = -\Omega_2^{\varphi,Q}$  for both bands.

moving average filter is applied to the data to decrease the noise level. A span of 5 values was chosen for the averaging. Raw data without averaging are provided in the Supplementary Material.

M.W. acknowledges financial support from the Erlangen Graduate School of Advanced Optical Technologies. Additionally, M.W. would like to thank Mark Kremer and Arstan Bisianov for fruitful discussions. Furthermore, this project was supported by DFG PE 523/14-1. H.M.P. was supported by the EC through the H2020 Marie Skłodowska-Curie Action, Individual Fellowship Grant No. 656093 SynOptic. I.C. was funded by the EU-FET Proactive grant AQuS, Project No. 640800, and by Provincia Autonoma di Trento, partially through the project “On silicon chip quantum optics for quantum

computing and secure communications (SiQuro)”.

\* For correspondence Ulf.Peschel@uni-jena.de

- [1] D. J. Thouless, M. Kohmoto, M. P. Nightingale, and M. den Nijs, *Physical Review Letters* **49**, 405 (1982).
- [2] M. Z. Hasan and C. L. Kane, *Reviews of Modern Physics* **82**, 3045 (2010), arXiv:1002.3895.
- [3] X.-L. Qi and S.-C. Zhang, *Reviews of Modern Physics* **83**, 1057 (2011), arXiv:1008.2026.
- [4] M.-C. Chang and Q. Niu, *Physical Review B* **53**, 7010 (1996), arXiv:9511014 [cond-mat].
- [5] D. Xiao, M.-C. Chang, and Q. Niu, *Reviews of Modern Physics* **82**, 1959 (2010).
- [6] L. Lu, J. D. Joannopoulos, and M. Soljačić, *Nature Photonics* **8**, 821 (2014), arXiv:1408.6730.
- [7] Z. Wang, Y. Chong, J. D. Joannopoulos, and M. Soljačić, *Nature* **461**, 772 (2009).
- [8] S. A. Skirlo, L. Lu, Y. Igarashi, Q. Yan, J. Joannopoulos, and M. Soljačić, *Physical Review Letters* **115**, 253901 (2015), arXiv:1504.04399.



- [9] L. Lu, Z. Wang, D. Ye, L. Ran, L. Fu, J. D. Joannopoulos, and M. Solja i, *Science* **349**, 622 (2015).
- [10] M. C. Rechtsman, J. M. Zeuner, Y. Plotnik, Y. Lumer, D. Podolsky, F. Dreisow, S. Nolte, M. Segev, and A. Szameit, *Nature* **496**, 196 (2013).
- [11] Y. E. Kraus, Y. Lahini, Z. Ringel, M. Verbin, and O. Zilberberg, *Physical Review Letters* **109**, 106402 (2012), arXiv:1109.5983.
- [12] T. Kitagawa, M. A. Broome, A. Fedrizzi, M. S. Rudner, E. Berg, I. Kassal, A. Aspuru-Guzik, E. Demler, and A. G. White, *Nature Communications* **3**, 882 (2012), arXiv:1105.5334.
- [13] M. Hafezi, S. Mittal, J. Fan, A. Migdall, and J. M. Taylor, *Nature Photonics* **7**, 1001 (2013).
- [14] S. Mittal, S. Ganeshan, J. Fan, A. Vaezi, and M. Hafezi, *Nature Photonics* **10**, 180 (2016), arXiv:1504.0369.
- [15] L. Duca, T. Li, M. Reitter, I. Bloch, and U. Schneider, *ArXiv*, 17 (2014), arXiv:1407.5635v1.
- [16] M. Atala, M. Aidelsburger, J. T. Barreiro, D. Abanin, T. Kitagawa, E. Demler, and I. Bloch, *Nature Physics* **9**, 795 (2013).
- [17] M. Aidelsburger, M. Lohse, C. Schweizer, M. Atala, J. T. Barreiro, S. Nascimbène, N. R. Cooper, I. Bloch, and N. Goldman, *Nature Physics* **11**, 162 (2014), arXiv:1407.4205.
- [18] G. Jotzu, M. Messer, R. Desbuquois, M. Lebrat, T. Uehlinger, D. Greif, and T. Esslinger, *Nature* **515**, 237 (2014), arXiv:1406.7874.
- [19] M. Mancini, G. Pagano, G. Cappellini, L. Livi, M. Rider, J. Catani, C. Sias, P. Zoller, M. Inguscio, M. Dalmonte, and L. Fallani, *Science* **349**, 1510 (2015).
- [20] B. K. Stuhl, H.-I. Lu, L. M. Ayccock, D. Genkina, and I. B. Spielman, *Science* **349**, 1514 (2015).
- [21] M. Lohse, C. Schweizer, O. Zilberberg, M. Aidelsburger, and I. Bloch, *Nature Physics* **12**, 350 (2015), arXiv:1507.02225v1.
- [22] S. Nakajima, T. Tomita, S. Taie, T. Ichinose, H. Ozawa, L. Wang, M. Troyer, and Y. Takahashi, *Nature Physics* **12**, 296 (2016), arXiv:1507.02223.
- [23] H.-I. Lu, M. Schemmer, L. M. Ayccock, D. Genkina, S. Sugawa, and I. B. Spielman, *Physical Review Letters* **116**, 200402 (2016), arXiv:1508.04480.
- [24] N. Flaschner, B. S. Rem, M. Tarnowski, D. Vogel, D.-S. Luhmann, K. Sengstock, and C. Weitenberg, *Science* **352**, 1091 (2016), arXiv:1509.05763.
- [25] T. Li, L. Duca, M. Reitter, F. Grusdt, E. Demler, M. Endres, M. Schleier-Smith, I. Bloch, and U. Schneider, *Science* **352**, 1094 (2016), arXiv:1509.00218.
- [26] H. M. Price and N. R. Cooper, *Physical Review A* **85**, 033620 (2012).
- [27] A. Regensburger, C. Bersch, M.-A. Miri, G. Onishchukov, D. N. Christodoulides, and U. Peschel, *Nature* **488**, 167 (2012).
- [28] A. Schreiber, K. N. Cassemiro, V. Potoček, A. Gábris, P. J. Mosley, E. Andersson, I. Jex, and C. Silberhorn, *Physical Review Letters* **104**, 050502 (2010).
- [29] M.-A. Miri, A. Regensburger, U. Peschel, and D. N. Christodoulides, *Physical Review A* **86**, 023807 (2012).
- [30] M. Wimmer, A. Regensburger, C. Bersch, M.-a. Miri, S. Batz, G. Onishchukov, D. N. Christodoulides, and U. Peschel, *Nature Physics* **9**, 780 (2013).
- [31] A. Regensburger, C. Bersch, B. Hinrichs, G. Onishchukov, A. Schreiber, C. Silberhorn, and U. Peschel, *Physical Review Letters* **107**, 233902 (2011).

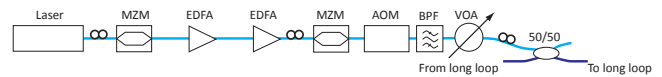


Figure 4. Signal generation. The signal of a DFB Laser is cut into a chain of 25 ns pulses by a Mach-Zehnder modulator (MZM), which is then amplified by two Erbium-doped fiber amplifiers (EDFA). A second MZM is used to suppress the background of the amplified pulse chain, which is adjusted in amplitude by a variable optical attenuator before the pulses are inserted into the fiber loops. An acousto-optical modulator (AOM) is set to full transmission during the warm-up phase and is set to total absorption after the last warm-up pulse, which is then the seed pulse for the measurement.

## Supplementary Information

### 1. Experimental setup

A linear version of the coupled fiber loop system presented in [30] is used. For the signal generation (see Fig. 4), a DFB laser diode operating at  $\lambda = 1555$  nm is cut into a chain of 25 ns long pulses by a Mach-Zehnder modulator (MZM). Afterwards, the pulses are amplified by two successive Erbium-doped fiber amplifiers (EDFA), before another MZM is set to zero transmission between two adjacent pulses in order to ensure a high suppression.

In the last stage, the pulses propagate through an acousto-optical modulator (AOM) and are cleaned by a bandpass filter before being injected into the longer fiber loop. At the beginning of the experiment, the AOM is set to a transmission of 100% allowing the pulse chain to enter the fiber loop system. After about 8 ms the system and especially the EDFAs are adapted to the input power level. When the last pulse has entered the system, the entrance AOM is set to full absorption.

Inside the coupled fiber loop system (see Fig. 5), the seed pulse first splits up at the 50/50 coupler connecting the longer and shorter loop. In each fiber ring, a wavelength division multiplexing coupler (WDM) is used to add a blue-shifted strong CW pilot signal operating at about 1537 nm into the fiber ring. The pilot signal maintains a constant amplification factor of the EDFAs in each loop and is removed from the signal by bandpass filters directly after the amplifiers. The pulses propagate through SSMF fiber spools with a length of about 1 km. In order to fine tune the length difference, SSMF patch cords are used. In total the average round trip time of both fiber loops is about 5200 ns while the length difference is chosen to be approximately 35 ns. The number of observable positions is equal to the ratio of both time constants  $n_{\max} = 5200/35 \approx 149$ . For monitoring the pulses circulating in the system a photodiode (PD) is attached to each loop via a 90/10 coupler. Furthermore, a single polarization is selected by a polarizing beam splitter in the longer loop. In the short loop, a phase modulator

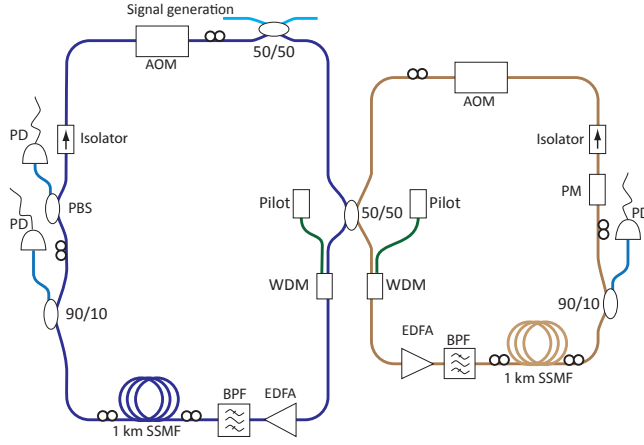


Figure 5. Sketch of the experimental fiber loop setup. Both fiber loops are connected by the 50/50 coupler. Any losses during one round trip are compensated in each ring by an Erbium-doped fiber amplifier (EDFA). In order to maintain a constant amplification rate, a pilot signal is inserted via a wavelength division multiplexing coupler (WDM) and afterwards removed by a bandpass filter (BPF). In order to establish a long average round trip time, each loop contains a 1 km long fiber spool followed by a 90/10 monitor coupler and a photo diode (PD). In the long loop, a polarizing beam splitter (PBS) is used to select a single polarization, while in the short loop a phase modulator (PM) allows for the generation of an arbitrary potential. An isolator prevents any back reflected light from circulating through the system. Acousto-optical modulators (AOM) at the end of each fiber ring are needed to block the circulation of pulses during the warm up phase.

(PM) is used to modulate the pulses according to Eq. 6 of the main paper and Eq. (S4) of the Supplementary Material. Finally, an AOM is placed in each fiber loop, which is set to zero transmission during the warm up phase, so that no pulses can recirculate through the fiber loops. When the entrance AOM is closed, the loop AOMs open and allow for the circulation of the initial seed pulse. Furthermore, the loop AOMs are used for the generation of Gaussian pulse trains as is explained in the Supplementary Material of [30].

## 2. Floquet band structure

Without any phase modulation, the size of the unit cell of the lattice depicted in Fig. 1a of the main part covers two rows and positions [27, 30]. For such a double step, the evolution is described by

$$2u_n^{m+2} = u_{n+2}^m + iv_{n+2}^m + iv_n^m - u_n^m \quad (12a)$$

$$2v_n^{m+2} = v_{n-2}^m + iu_{n-2}^m + iu_n^m - v_n^m. \quad (12b)$$

Since the system is evolving in discrete time steps, denoted by the superscript  $m$ , on a discrete lattice, with

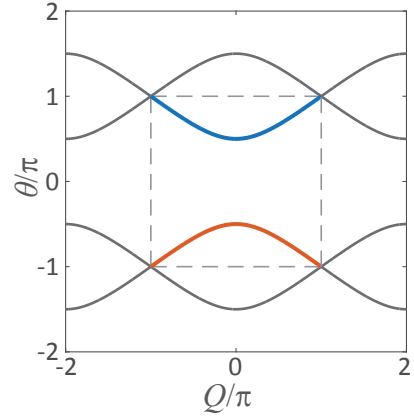


Figure 6. Dispersion relation of the unmodulated system. Due to the temporal periodicity of the system after two round trips, the band structure is periodic in the Bloch momentum  $Q$  and the propagation constant  $\theta$ . The first Brillouin zone is highlighted by the dashed gray rectangle.

sites labelled by  $n$ , we apply a Floquet Bloch ansatz of the form [27, 29, 30]

$$\begin{pmatrix} u_n^m \\ v_n^m \end{pmatrix} = \begin{pmatrix} U \\ V \end{pmatrix} e^{-i\theta m/2} e^{iQn/2} \quad (13)$$

The resulting dispersion relation (see Fig. 6)

$$\cos \theta = \frac{1}{2}(\cos Q - 1) \quad (14)$$

consists of two bands separated by a band gap. However, due to the Floquet nature of the system, the band structure is not only periodic in  $Q$  but also in  $\theta$  and as a result both bands intersect for  $Q = \pm\pi$  and  $\theta = \pm\pi$  (see Fig. 6). The two component vector  $(U, V)^T$  stands for the eigenstate corresponding to a given value of  $\theta$  and  $Q$ , and which therefore is determined by the phase- and amplitude-relation between the short and long loop. In good approximation, an eigenstate is excited by generating a Gaussian beam in both loops and by setting the appropriate phase relation S1. According to the size of the unit cell, the natural time scale along the propagation direction covers two time steps.

## 3. Band structure of the modulated system

In order to implement the geometrical “pumping”, a phase modulation  $\Phi$  is applied to the short loop according to

$$\Phi(M(m)) = \begin{cases} -\varphi(M(m)) & \text{odd } m \\ +\varphi(M(m)) & \text{even } m \end{cases} \quad (15)$$

where the sign alternates after each single time step  $m$ . For a constant modulation amplitude  $\varphi$ , the dispersion

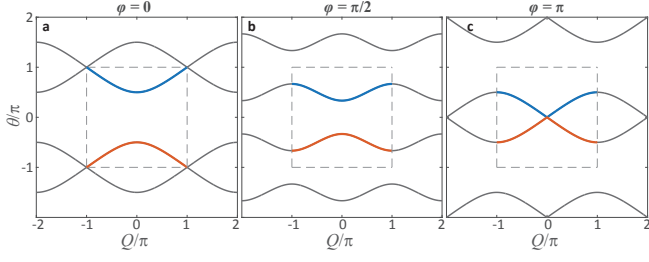


Figure 7. Band structure of the temporal driven system. a-c, Band structure of the system driven by the two step modulation for  $\varphi = 0$ ,  $\varphi = \pi/2$  and  $\varphi = \pi$ . For  $\varphi = \pi$  band gap is closed at the center of the Brillouin zone.

relation reads as

$$\cos \theta = \frac{1}{2}(\cos Q - \cos \varphi) \quad (16)$$

The band structure is depicted in Fig. 7 for different values of  $\varphi$ .

By introducing the temporal modulation schemes explained above, the dispersion relation now not only depends on the Bloch momentum  $Q$ , but also on the phase amplitude  $\varphi$ . In the main part of the publication,  $\varphi$  is swept during the propagation, equivalent to a temporal driven system known as geometrical “pumping”. Thus, the height of the phase modulation

$$\varphi(M(m)) = \varphi_0 M(m) \quad (17)$$

is increased after every modulation period  $M(m) = \lfloor m/2 \rfloor$ , as depicted in Fig. 8 for a phase gradient  $\varphi_0 = \pi/16$ . Here, the comparatively large gradient is only chosen to make the scheme more clear; in the experiment, a much smaller phase gradient of  $\varphi_0 = \pi/100$  is used to ensure that the wave packet moves adiabatically for most values of the Bloch momentum  $Q$ . This fails close to the band-degeneracies where adiabaticity breaks down and there can be transitions between bands. Other limitations in the applicability of our protocol to measure the Berry curvature are discussed in Supplementary Note S5.

#### 4. Explanation of the experimental protocol

We consider the dynamics of a semi-classical wave packet, prepared in a single band  $j$ , with a well-defined center-of-mass position  $n$  and center-of-mass momentum  $Q$ . In order to understand the dynamical evolution of the system, we first review the case for the modulated system described by Eq. (15), where the phase amplitude  $\varphi = \text{const}$ . Then, the total velocity at which the wave packet travels is given by the group velocity of the band

$$v_j^G(\varphi, Q) = \frac{\partial}{\partial Q} \theta_j(\varphi, Q). \quad (18)$$

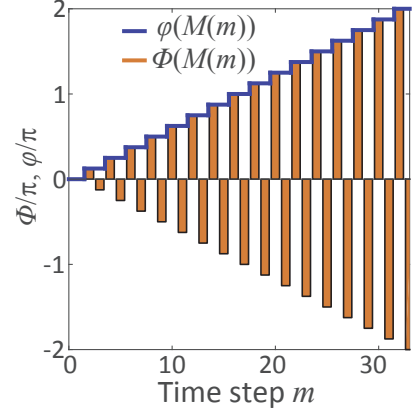


Figure 8. Illustration of the phase modulation for a gradient  $\varphi_0 = \pi/16$ . The applied phase  $\Phi(m)$  alternates between  $\pm\varphi(m)$  after each roundtrip (see the orange bars), while the amplitude of the phase modulation  $\varphi(m)$  increases only after every second time step (see the blue stair function).

After  $M$  periods, the center-of-mass position of the wave packet is given by the integral over the group velocity

$$n_j(M) = \int_0^M v_j^G(\varphi, Q) dM' = v_j^G(\varphi, Q) M. \quad (19)$$

Now, we consider the modulation protocol described by Eq. 17 where the phase amplitude is gradually ramped up. Then, not only does the group velocity change according to the phase  $\varphi(M(m))$ , but the wave packet also gains an anomalous velocity due to the Berry curvature, leading to a total velocity[5, 26] of

$$v_j(Q, \varphi) = v_j^G(\varphi(M), Q) + \varphi_0 \Omega_j^{\varphi(M), Q}, \quad (20)$$

where hereafter we drop the explicit dependence on  $m$  for simplicity of notation. The Berry curvature is calculated numerically by evaluating the expression

$$\Omega_j^{\varphi(M), Q} = i \frac{\partial}{\partial \varphi} \left\langle \psi_j \left| i \frac{\partial}{\partial Q} \right| \psi_j \right\rangle - i \frac{\partial}{\partial Q} \left\langle \psi_j \left| i \frac{\partial}{\partial \varphi} \right| \psi_j \right\rangle, \quad (21)$$

where  $\psi_j = (U_j, V_j)^T$  is the eigenstate of a band, as defined in the ansatz of Eq. (13).

In the experiment, we excite a wave packet centered around a specific Bloch momentum by using the modulation scheme described in the Supplementary Material Note 1.6 of [30]. Then the wave packet propagates through the lattice under an external phase gradient of either  $+\varphi_0$  or  $-\varphi_0$ . For both cases, the center-of-mass  $n_j(M)$  is evaluated for integer multiples of the modulation period  $M$ , so that we can extract the difference in



the center-of-mass shift:

$$n_j^{+\varphi_0}(M) - n_j^{-\varphi_0}(M) = \int_0^M [v_j(Q, +\varphi_0 M') - v_j(Q, -\varphi_0 M')] dM' \quad (22)$$

between a positive and negative phase gradient  $\varphi_0$ . Evaluating Eqn. 21 and 22 leads to the final expression

$$n_j^{+\varphi_0}(M) - n_j^{-\varphi_0}(M) = \int_0^M 2\varphi_0 \Omega_j^{\varphi(M'), Q} dM' \quad (23)$$

$$\Omega_j^{\varphi(M), Q} = \frac{n_j^{+\varphi_0}(M+1) - n_j^{+\varphi_0}(M-1) - (n_j^{-\varphi_0}(M+1) - n_j^{-\varphi_0}(M-1))}{4\varphi_0}. \quad (24)$$

## 5. Restrictions on the protocol

In general, there are two conditions on the underlying model, which need to be fulfilled in order to apply the protocol described above. For the derivation of Eq. 24 it was assumed that the group velocity and the Berry curvature are symmetric in  $\varphi$

$$v_j^G(\varphi, Q) = v_j^G(-\varphi, Q) \text{ and } \Omega_j^{\varphi, Q} = \Omega_j^{-\varphi, Q}. \quad (25)$$

For our modulation scheme, these conditions are fulfilled as a change in the sign of  $\varphi$  is equivalent to a shift of the modulation by one time step (see Fig. 9). The band dispersion and Berry curvature, however, are gauge-invariant under this transformation and so Eq. (25) follows. In the case of a modulation scheme where these conditions are not satisfied, a more general protocol according to [26] should be chosen, where the wave packet velocity is compared at the same value of  $(\varphi, Q)$ , under positive and negative phase gradients. Whenever our scheme [Eq. (23)] is applicable, it has the key advantage over the general protocol [26] that the extracted Berry curvature is less affected by band degeneracies and the corresponding breakdowns in adiabaticity. To see this, consider a band which is degenerate with a second band at some parameters  $(\varphi_1, Q_1)$ , and hence, by the symmetry implied by Eq. (25), also at parameters  $(-\varphi_1, Q_1)$ . In our scheme, we compare the propagation of wave packets after a given number of modulation steps, under opposite phase gradients [Eq. (23)]. This approach works well until the wave packets reach the band degeneracies where the evolution is no longer adiabatic; for both negative and positive phase gradients, this occurs after  $M_1 = \varphi_1/\varphi_0$  modulation periods. In the more general protocol, we compare the motion of the wave packets at the same value of  $(\varphi, Q)$ , corresponding to  $M^+(\varphi_0) = \varphi/\varphi_0$  modulation periods for the positive

where we have used that  $v_j^G(\varphi, Q) = v_j^G(-\varphi, Q)$  and  $\Omega_j^{\varphi, Q} = \Omega_j^{-\varphi, Q}$  (see Section S5). Therefore, the integral of the Berry curvature is given by the lateral shift of the measured center-of-masses. To reconstruct the total Berry curvature, the center-of-mass shift is numerically differentiated in order to find

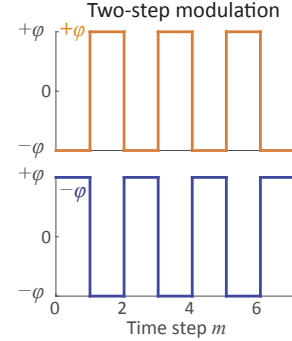


Figure 9. Comparison of the modulation for  $\pm\varphi$  without any phase gradient. The change in sign of  $\varphi_0 \rightarrow -\varphi_0$  is equivalent to a shift of the modulation by one time step  $m \rightarrow m+1$ .

phase gradient and  $M^-(\varphi_0) = (2\pi - \varphi)/\varphi_0$  modulation periods for the negative phase gradient. As always either  $M^{+\varphi_0} > M_1$  or  $M^{-\varphi_0} > M_1$ , this method breaks down for any Bloch momentum,  $Q_1$ , for which a band degeneracy occurs somewhere in the 2D parameter space.

## 6. Evaluation of the experimental data

In order to extract the center-of-mass during the propagation, a Gaussian distribution was fitted to each measurement for every second time step, for each Bloch momentum  $Q$  (see Fig. 10). In some cases, not only one band is excited, but also the other, leading to a secondary wave packet propagating in the opposite direction (see Fig. 11c,h) due to the opposite group velocity and Berry curvature in the upper band. The reason for this imperfection can be due to a mismatch of the initial state with the required eigenstate and to the adjacency

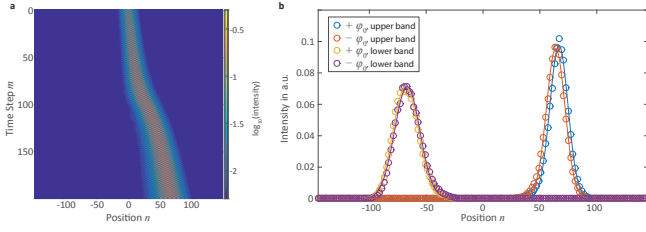


Figure 10. Example of the propagation of a wave packet and extraction of the center-of-mass. a, Wave packet propagation for  $Q = 0.1\pi$  in the upper band for  $\varphi_0 = +\pi/100$ . b, Extracted experimental cross section, for the last time step  $m = 200$ , for the upper and lower band and for  $\pm\varphi_0$ . In order to extract the center-of-mass for each measurement, Gaussian fits (solid lines) are applied to the experimental data points (circles).

of band-degeneracy points.

For extracting the center-of-mass, a Gaussian distribution of the form

$$f(n) = Ae^{-\frac{(n-n_0)^2}{C^2}} \quad (26)$$

is fitted to the intensity distribution for each time step. To initialize the fit,  $n_0$  is set to the location of the maximum,  $C$  to the approximate width of 5.6 positions, which is equivalent to the spatial width of the wave packet in the first time step, and  $A$  is set to the maximum intensity per time step. By extracting the error margins of the fit parameter  $n_0$  for a confidence interval of 95% it is possible to estimate the uncertainty of this procedure and so to calculate  $\Delta n_j^{\pm\varphi_0}$ : the uncertainty of the fit for the positive and negative phase modulation. The total uncertainty in the integrated Berry curvature due to the fit is thus given by  $\sqrt{(\Delta n_j^{+\varphi_0})^2 + (\Delta n_j^{-\varphi_0})^2}$ , while the uncertainty with respect to  $Q$  is estimated by the spectral width  $\Delta Q$  of the wave packet, as determined by numerically Fourier transforming the initial distribution. Here, a value of approximately  $\Delta Q \approx 0.066\pi$  is found for the FWHM of the intensity for all data sets.

By using this protocol, the integrated Berry curvature is directly observed. However, to reconstruct the Berry curvature itself, it is necessary to differentiate the experimental results numerically. Since this procedure is very sensitive to noise, the experimental data is first smoothed by an averaging filter spanned over five elements. The influence of the averaging filter is shown in Figure 12.

## 7. Spectral width of the wave packet

All experiments which are discussed in the manuscript are carried out with a wave packet covering approximately 6 positions in real space corresponding to a spectral width of  $0.07\pi$ . In our semi-classical analysis, we assume that the wave packet propagates like a classical

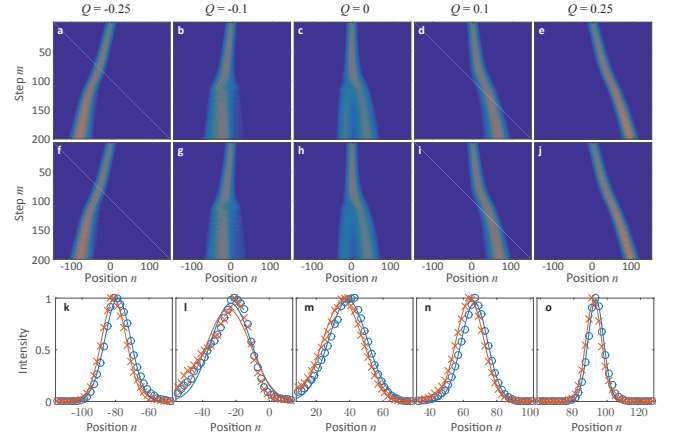


Figure 11. Experimental propagation for the two-step modulation for the upper band. Measurement of a wave packet in the upper band for  $-\varphi_0$  (a-e) and for  $+\varphi_0$  (f-j) over 200 time steps. At each time step, the center-of-mass is estimated by applying a Gaussian fit to the cross section. (k-o) As an example of this procedure, the cross sections and fitted curves are displayed at the last time step for  $-\varphi_0$  (red) and for  $+\varphi_0$  (blue).

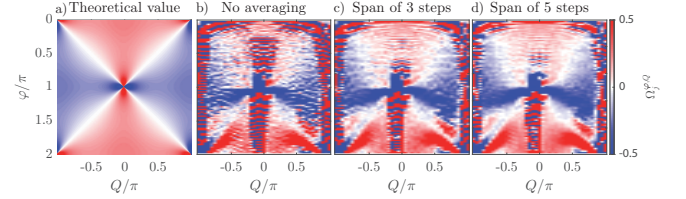


Figure 12. Influence of the averaging on the reconstruction of the Berry curvature. High frequency noise due to experimental imperfections is reduced by an averaging filter. In Figure 3 of the manuscript, the filter spans 5 data points (d) which effectively suppresses the noise that it is inevitably present in the raw data (b).

particle with a well-defined group velocity that is shifted by the anomalous velocity due to the Berry curvature. However, this description is no longer applicable if the wave packet becomes too spectrally broad in momentum, as then it is no longer sufficient to characterize the motion of the wave packet by one value of the Bloch momentum  $Q$ . In order to investigate the dependence of our results on the width of the wave packet, the measurement has been reproduced in simulations for wave packets of different width (see Fig. 13).

## 8. Anomalous transport for the four time step modulation

In order to demonstrate the general applicability of the experimental protocol, a second modulation scheme is discussed in this section. It is designed in the same

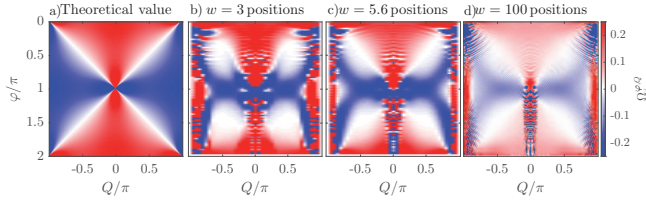


Figure 13. Dependence on the spectral width of the wave packet (simulation). While the basic characteristics of the Berry curvature (a) are already recovered by a wave packet with a width,  $w$ , of only 3 positions in real space (b), the resolution is sharpened with growing width of the wave packet, as this corresponds to a narrower spread in Bloch momenta. In the experiment, similar parameters to those (c) are used; the width here of 5.6 positions in real space corresponds to a spectral width of  $0.07\pi$ , with the Bloch momentum scanned in steps of  $0.05\pi$ . For (b,c) the same gradient  $\varphi_0 = \pi/100$  is used, while in (d) a smaller gradient  $\varphi_0 = \pi/200$  and a finer discretization of  $Q$  in steps of  $0.01\pi$  is chosen. Additionally, in (d) the averaging filter spans 19 time steps.

way as the previous modulation and differs only in the internal length of the modulation scheme. For the second modulation

$$\Phi_{4\text{step}}(M(m)) = \begin{cases} -\varphi(M(m)) & \text{mod}(m, 4) = 0 \text{ or } 1 \\ +\varphi(M(m)) & \text{mod}(m, 4) = \text{else} \end{cases} \quad (27)$$

where now the modulation period  $M(m) = \lfloor m/4 \rfloor$  lasts for four time steps. Therefore, the dispersion relation is calculated for one modulation period using the ansatz

$$\begin{pmatrix} u_n^m \\ v_n^m \end{pmatrix} = \begin{pmatrix} U \\ V \end{pmatrix} e^{-i\theta m/4} e^{iQn/4}. \quad (28)$$

In this case, the dispersion relation reads as

$$\cos \theta = \frac{1}{4}(\cos 2Q - \cos 2\varphi - 4 \cos Q \cos \varphi). \quad (29)$$

Interestingly for  $\varphi = 0$ , when no modulation is present, the size unit cell collapses again to two time steps, hence the band structure represented by Eq. (S18) is artificially back-folded (compare also with Fig. 7a and d). This aspect is further illustrated by comparing the band structure for  $\varphi = 0$  given by Eq. (14) and Eq. (29).

As one can see, for the four time step ansatz, this back-folding leads to a closing of the band gap, which is not physically-motivated but instead an artefact of the chosen ansatz in Eq. (28). However, for any finite phase modulation  $\varphi \neq 0$ , the four time step ansatz is needed in order to cover the whole modulation period. The dispersion relation for the four-step modulation is shown in Fig. 14a and b for various values of  $\varphi$ .

By applying the procedure for the two-step modulation also for the four-step scheme, the results presented in Fig. 14 are obtained. The back-folding of the band structure along  $\theta$  leads to additional singularities in the case of the

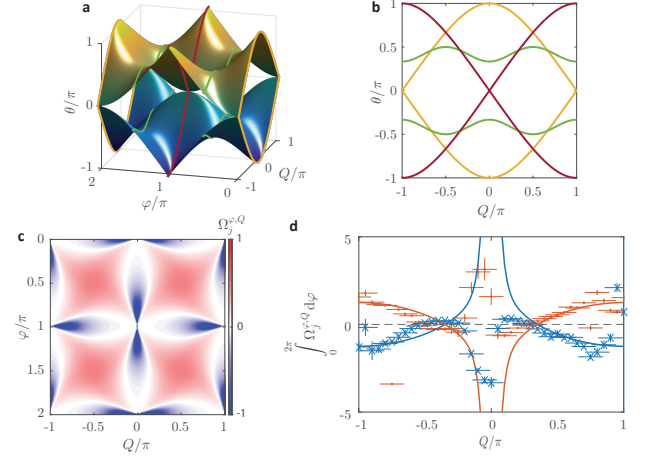


Figure 14. Anomalous transport for the four-step modulation. a, Band structure of the system. As for the two-step modulation, the band structure is also periodic in  $\theta$ . b, Cut through of the dispersion relation for  $\varphi = 0$  (yellow),  $\varphi = \pi/2$  (green) and  $\varphi = \pi$  (red). Compared to the two-step modulation, additional band-degeneracy points are present, as also visible as singularities in the plot of the Berry curvature for the upper band (c). d, Measured integrated Berry curvature for the four-step modulation for the upper band (orange dots) and the lower band (blue crosses). Again, close to the singularities, the protocol fails as adiabaticity breaks down.

Berry curvature (see Fig. 14a-c). For the propagation in real space, the touching of the bands leads to an emission of a smaller counter-propagating secondary wave; to account for this, we fit the propagation cross-section with a double Gaussian profile, instead of a single Gaussian as in Eq. (26), taking the center of the higher Gaussian peak as the center-of-mass position. In this way, we can again extract the integrated Berry curvature, as shown in Fig. 14d.